Contemporary Mathematics
https://ojs.wiserpub.com/index.php/CM/

UNIVERSAL WISER
PUBLISHER

Research Article

Implementation of Advanced SVPWM Control Algorithms for Switch State Management in a Multilevel Cascaded Inverter within an Electric Traction Chain

Abdellah Oukassi

National School of Applied Sciences, Systems & Applications Engineering Laboratory (LISA), Cadi Ayyad University, Marrakesh, 40000, Morocco
E-mail: abdououkassi16@gmail.com

Received: 10 July 2025; **Revised:** 5 August 2025; **Accepted:** 21 August 2025

Abstract: This paper presents the development of advanced Space Vector Pulse Width Modulation (SVPWM) algorithms based on newly formulated mathematical models, aimed at controlling the switching states of multilevel cascaded inverters. The proposed control scheme introduces a generalized layer-based decomposition methodology with any number of levels n. By leveraging this hierarchical framework, the method achieves a substantial reduction in Total Harmonic Distortion (THD), lowering it from approximately 50% to below 10%, and ensuring the generation of high-quality, near-sinusoidal output waveforms. These algorithms are integrated into an electric traction system powered by photovoltaic energy sources. The actuator used in this chain is an induction motor controlled in a vector manner. The layered structure allows the systematic identification of all possible vectors per layer, the determination of redundant vectors, and the classification of distinct and equivalent switching states across the entire modulation space. A dedicated coding system assigns a unique identifier to each vector, allowing efficient tracking of corresponding redundant vectors on the layers. This redundancy management framework improves modulation flexibility and allows a transition between equivalent states. Moreover, the process of decomposition of a global reference voltage into its multilevel components is addressed by the analytical determination of amplitudes and transition angles. This contributes to a computationally efficient, modular modulation structure that significantly reduces implementation complexity and enables real-time application. The proposed algorithms have been validated by complete simulations in the MATLAB/Simulink environment. The results demonstrate superior performance in terms of output waveform quality, harmonic suppression, and switching loss reduction, highlighting the appropriateness of the approach for high-efficiency traction systems based on renewable energies.

Keywords**:** layer-based control, multilevel inverter, Space Vector Pulse Width Modulation (SVPWM), induction motor, photovoltaic generators, Indirect Field-Oriented Control (IFOC), Proportional Integrator (PI) controller, redundant vectors

MSC: 93C10, 93C83

DOI: https://doi.org/10.37256/cm.6520257796

1. Introduction

In high-power applications, multilevel converters have emerged as a preferred solution for electrical energy conversion, enabling the generation of quasi-sinusoidal alternating voltage from continuous Direct Current (DC) sources [1]. Their integration spans across various industrial domains, including automotive, aerospace, and railway systems [2], where their adoption is steadily growing. Despite their reliability and increasing use, multilevel converters still present several technical challenges, such as controlling harmonic distortion, reducing energy losses, and implementing more efficient control strategies. Far from being limiting factors, these challenges are viewed as catalysts for innovation, fostering ongoing research and development in the field of power electronics and energy conversion.

Extensive research has been devoted to multilevel converters, highlighting their increasing prominence in high-power energy conversion applications. Notable investigations have focused on classical topologies such as the Neutral Point Clamped (NPC) converter [3], the Flying Capacitor (FC) converter [4], and the Cascaded H-Bridge (CHB) converter [5]. A particularly noteworthy recent study presents the design and implementation of a six-level NPC inverter integrating Selective Harmonic Elimination (SHE) techniques. Tailored for railway traction systems, this inverter operates at a DC input voltage of approximately 1,500 V and has demonstrated efficiency gains exceeding 5% relative to conventional two-level inverter counterparts [1]. In parallel, Modular Multilevel Converters (MMCs) have been proposed for railway traction applications [2], focusing on harnessing regenerative energy through high-voltage supercapacitor energy storage. This approach significantly enhances overall system efficiency and energy management compared to traditional two-level converter architectures by enabling improved power quality and effective energy recuperation. The key characteristics of multilevel inverters [6] include their ability to generate output voltage pulses with lower amplitude steps compared to traditional two-level inverters, resulting in significantly improved output voltage quality. This enhancement reduces the size and complexity of filter inductors required to meet electromagnetic compatibility standards. Additionally, by producing output voltages with minimized harmonic distortion, multilevel inverters alleviate dv/dt stress on power devices [6]. These inverters offer flexible switching frequency capabilities, simultaneously operating at both the fundamental frequency and higher PWM carrier frequencies, akin to conventional inverter technologies. Moreover, multilevel inverters efficiently handle input currents while maintaining low distortion, thereby improving overall system energy efficiency.

The topologies mentioned above are primarily distinguished by their switching mechanisms and input voltage sources. By tailoring these configurations to meet the specific demands of various industrial applications, their performance can be optimized, thereby fostering wider adoption across multiple sectors. Below, we summarize some of the most employed topologies. The NPC converter architecture stands as a fundamental benchmark in multilevel conversion, originally developed by Hirofumi Akagi and Akira Nabae in 1981. Its primary objective is to reduce the Total Harmonic Distortion (THD) injected into the load, particularly in motor drive applications. The NPC topology is extensively utilized in renewable energy systems [7], notably in Photovoltaic (PV) installations supplying the DC bus, as well as in the control of induction motors. The FC inverter, introduced by Meynard and Foch in 1992, represents a significant advancement in multilevel converter design. While this topology resembles that of multilevel inverters employing blocking diodes, it innovatively replaces these diodes with capacitors, providing the equilibrium voltages [8]. The main objective of this innovation is to overcome the voltage balancing problems encountered in the NPC topology while minimizing the number of diodes needed. The CHB converter is a widely adopted multilevel converter topology, extensively used in high-power energy conversion applications [9, 10]. The CHB architecture consists of multiple series-connected H-bridge modules, each capable of generating distinct voltage levels. Each module can be independently controlled, enabling precise modulation of the overall output voltage. The total output voltage is obtained by the superposition of the voltages from each H-bridge module, allowing the generation of an output waveform with significantly higher levels than a conventional two-level inverter. The CHB topology finds applications across various fields, including photovoltaic systems for grid energy injection, Alternating Current (AC) machine control in variable speed drives, and traction systems for trains and electric vehicles [10]. In this work, we adopt the cascaded topology powered by photovoltaic cells.

In practice, these multilevel inverters require sophisticated control techniques to generate the precise gating signals needed to drive the inverter. This enables the output voltage waveform to closely approximate an ideal sinusoid. Over the past three decades, various Pulse Width Modulation (PWM) controllers have been developed for industrial applications, each offering specific advantages in terms of waveform quality, system loss reduction, and efficiency enhancement [11]. These advancements have significantly contributed to improving the overall performance of electrical systems. Among the most widely used methods are Sinusoidal Pulse Width Modulation (SPWM) and Space Vector PWM (SVPWM). Both techniques are distinguished by their ability to improve output voltage quality while minimizing distortions. However, traditional SPWM is primarily designed for two-level inverters, limiting its applicability in multilevel configurations. To overcome these limitations, the Multi-Carrier PWM (MCPWM) technique was introduced. MCPWM aims to reduce harmonic distortion in output waveforms, enable low-frequency operation, optimize DC bus voltage utilization, and mitigate switching device stress [12]. The core principle of MCPWM relies on employing multiple triangular carrier signals, which are compared against a single sinusoidal reference waveform to generate switching pulses. Among the most recognized MCPWM variants are Phase Disposition (PD), Phase Opposition Disposition (POD), and Alternative Phase Opposition Disposition (APOD) schemes [13]. SVPWM was initially developed for the control of induction and brushless motors [14]. Compared to conventional SPWM, SVPWM presents several key advantages, particularly in its ability to generate higher output voltage amplitudes. SPWM depends on multiple carrier signals. SVPWM removes this requirement by directly synthesizing the reference voltage vector using a set of predefined switching vectors. Each switching vector represents a distinct switching state configuration of the three-phase inverter.

There are several modulation methods, including SHE. This method is based on a mathematical analysis based on the Fourier series decomposition of the inverter output signal. It consists in calculating optimal switching angles to suppress certain precise harmonics, such as those of order 5, 7, 11 or 13. These angles are often obtained through optimization techniques, such as the Bird Swarm Algorithm (BSA) [15]. One of the great advantages of this method is that it achieves a very low THD rate, especially at low frequencies, while effectively suppressing unwanted harmonics. That is why it is often used in applications sensitive to signal quality, such as electric traction or wind systems. However, this method also has disadvantages. Its real-time implementation is difficult, because it requires either storing angle tables in advance or performing complex calculations in real time, which can require a lot of resources. The second method, based on the notion of layers, is a control strategy used for multilevel inverters. It applies within the framework of SVPWM modulation, exploiting the transition between several hexagons, each representing a different layer. Its principle is based on the selection, at each moment, of the switching vector whose amplitude and angle are closest to those of the reference voltage vector. The vector diagram of the inverter is generally structured in hexagonal layers, which allows the algorithm to restrict the search to the relevant layers, depending on the position of the vector to be reproduced. This method has several important advantages. It is simple to implement and requires a reduced computation time, which makes it particularly suitable for real-time implementation, especially on Digital Signal Processor (DSP) or Field-Programmable Gate Array (FPGA) platforms. In addition, it offers great flexibility, allowing efficient management of redundancies and thus contributing to limiting losses. This article explores vector modulation techniques for CHB multilevel inverters, based on the concept of layers. We introduce novel mathematical expressions, presented here for the first time. These formulations will assist researchers in implementing control algorithms for inverter levels ranging from 5 to 15. The developed algorithms will be implemented and tested in a closed-loop variable speed drive.

2. Topology of a cascaded type of multi-level inverter

The cascaded inverter is known by several names, including "Cascaded H-Bridge multilevel inverter" or "Multicellular cascaded multilevel inverter." Its main advantage lies in its modular structure. It consists of multiple H-bridge inverter modules connected in series for each phase, depending on the desired number of levels [16]. Each module can be repeated as many times as necessary to achieve the desired output voltage level. The inverter is powered by multiple independent DC voltage sources, such as fuel cells, batteries, or photovoltaic cells. The overall output voltage is obtained by summing the output voltages of the different modules, which are connected in series [16]. Figure 1 illustrates the conventional topology of an n-level CHB inverter. This architecture is based on cascading single-phase H-bridge inverter modules. For each phase, $\dfrac{n-1}{2}$ modules are used, each supplied by an independent and isolated DC voltage source. Therefore, the total number of required sources is $\frac{n-1}{2}$ in a phase. Regarding the total number of IGBT/diode switches [12], it amounts to $2(n-1)$.

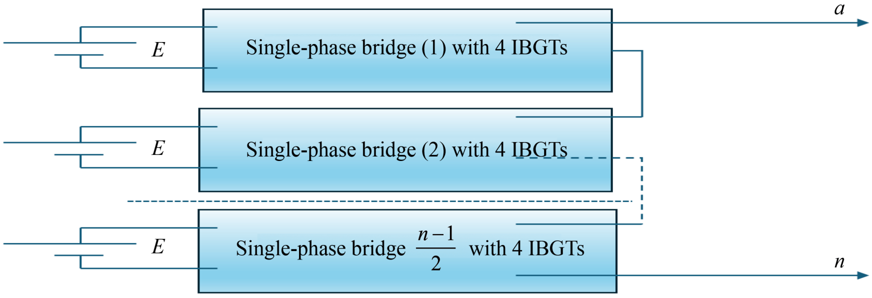

Figure 1. Structure of an n-level inverter (a single phase)

3. SVPWM: new design and modelling

Existing methodologies.

According to article [17], an n-level cascaded converter consists of $(n-1)$ layer, each bounded by a hexagon. On these hexagons, the reference vectors can be located by first calculating their amplitude and phase in the (α, β) reference frame. The vector diagram associated with an n-level inverter contains $(n-1)^3$ triangles [17]. Still within the scope of the literature, the authors of the article, as an example, studied the case of a five-level inverter. They assigned codes to the reference vectors ranging from (4)(0)(0) to (0)(0)(0), then decomposed the five-level vector diagram into a three-level diagram. The latter was further decomposed into a two-level diagram by using appropriate transition expressions between the different levels. Similarly, the authors of the article [17] proposed an SVPWM control strategy for a seven-level inverter. Their approach involves decomposing the seven-level vector diagram into a four-level diagram, then into a two-level diagram, introducing transition expressions between these structures. However, they do not explicitly detail the coding principle of the vectors on the seven-level diagram. The Articles [18, 19] present a similar method for a nine-level inverter, successively decomposing the nine-level diagram into a five-level diagram, then into a two-level diagram. In this case as well, transition expressions between levels are proposed, although they are not always accompanied by a complete justification of the coding logic.

Methodology for designing an SVPWM control algorithm for n levels.

An n-level inverter presents $\frac{n-1}{2}$ voltage levels during the positive half-cycle and $\frac{n-1}{2}$ levels during the negative half-cycle, with a zero-level positioned between the two half-cycles. Thus, it has a total of n distinct output voltage levels. In the case of a three-phase n-level inverter, the total number of possible switching combinations is equal to n^3. This means that n^3 reference vectors can be generated. Denoting Fk as the code assigned to each phase (where k represents phase a, b, or c), and assuming that voltage level is numbered from 1 to n (as shown in Table 1), it is then possible to determine all combinations of voltage levels for the three phases. Each vector is associated with a code composed of three digits (Fa, Fb, Fc) corresponding to the voltage levels of phases a, b, and c. For the n^3 possible vectors, the codes range from $(n, 1, 1)$ down to $(1, 1, 1)$.

Table 1. The table showing the number assigned for each level and possibly the level of each voltage at the output of a three-phase multilevel inverter

Sa, Sb, Sc	$\frac{n-1}{2}$	$\frac{n-1}{2}-1$	...	0	...	$-\frac{n-1}{2}+1$	$-\frac{n-1}{2}$
Fa, Fb, Fc	n	$n-1$	...	$\frac{n-1}{2}+1$	...	2	1

For example, for the combination n11 ($Fa = n, Fb = 1, Fc = 1$), we match the following different levels: For phase a: we have: $Va = +\frac{n-1}{2} \cdot E$, For phase b we have: $Vb = -\frac{n-1}{2} \cdot E$, and for phase c, we: $Vc = -\frac{n-1}{2} \cdot E$.

For each switching code among the n^3 possible combinations, it is necessary to assign the corresponding voltage level to each of the three phases (a, b, and c), according to Table 1. Then, the phase voltages concerning the system's neutral point are calculated. Once these voltages are determined, the Concordia transformation (also known as the $\alpha - \beta$ transformation) is applied to obtain the components of the voltage vector in the $(\alpha,\ \beta)$ plane. This enables the evaluation of both the angular phase and amplitude of each vector, as well as its angular position. With this information, each vector can be precisely located within the n-level vector diagram: that is, identifying the specific "layer" or hexagon in which it lies. Using a database established in Excel for various multilevel inverter configurations (5, 7, 9, 11, and 15 levels), we determined the position of each vector in the $(\alpha,\ \beta)$ reference frame by calculating their amplitude and angular phase. Analysis of this database allowed us to identify redundant vectors within each layer of the vector diagram: that is, vectors with identical coordinates but resulting from different switching combinations. With this information, it is possible to determine: the total number of redundant vectors, the total number of distinct vectors, the total number of non-zero vectors, and the number of zero vectors. Table 2 presents an extract of the data obtained for a nine-level inverter (n = 9). In this table, Sc (where k denotes phase a, b, or c) represents the voltage level delivered to the output of the series-connected H-bridges in each phase. The phase voltages concerning the neutral point, noted respectively as v_{an}, v_{bn}, and v_{cn}, are calculated from the indices S_{an}, S_{bn}, S_{cn} according to the following relationships (1):

$$\begin{bmatrix} v_{an} \\ v_{bn} \\ v_{cn} \end{bmatrix} = \begin{bmatrix} \frac{2}{3} & -\frac{1}{3} & -\frac{1}{3} \\ -\frac{1}{3} & \frac{2}{3} & -\frac{1}{3} \\ -\frac{1}{3} & -\frac{1}{3} & \frac{2}{3} \end{bmatrix} \cdot \begin{bmatrix} V_a \\ V_b \\ V_c \end{bmatrix} \tag{1}$$

Where E represents the elementary voltage of each module. These voltages can then be converted to coordinates $(\alpha,\ \beta)$ via the Concordia transformation, which allows analysing the output vectors in the vector plane ($V\alpha = K\alpha \times E$, $V\beta = K\beta \times E$, $\boxed{Kref^2 = K\alpha^2 + k\beta^2}$ and $Vref = Kref \times E$).

$$\text{With} \quad \begin{bmatrix} V_a \\ V_b \\ V_c \end{bmatrix} = \begin{bmatrix} S_a \\ S_b \\ S_c \end{bmatrix} \cdot E \quad \text{and} \quad \begin{bmatrix} V_{an} \\ V_{bn} \\ V_{cn} \end{bmatrix} = \begin{bmatrix} S_{an} \\ S_{bn} \\ S_{cn} \end{bmatrix} \cdot E$$

The analysis of the data presented in Table 3 leads to several important conclusions regarding the structure of the vector diagram in the $(\alpha,\ \beta)$ plane, particularly the distribution of vectors across the different hexagonal layers. In the outermost layer, corresponding to layer $(n-1)$, there are 6 × $(n-1)$ distinct vectors with no redundancy. The factor 6 corresponds to the number of sides of the hexagon, which remains constant across all layers due to the regular hexagonal geometry. In layer $(n-2)$, each distinct vector has two redundancies. Therefore, the number of distinct vectors is 6 × $(n-2)$, and the total number of vectors (including redundancies) is 6 × $(n-2)$ × 2. More generally, for layer $(n-i)$, each vector has (i) redundancies. The number of distinct vectors in that layer is 6 × (ni), and the total number of vectors (including redundancies) is 6 × $(n-i)$ × (i). In layer 1, each vector has $(n-1)$ redundancies. The number of distinct vectors is 6 × 1, and the total number of vectors in this layer is 6 × $(n-1)$. Finally, layer 0 corresponds to the zero vector, located at the origin of the $(\alpha,\ \beta)$ plane. This layer contains n redundant vectors, representing all the combinations. *Tapez une quation ici.* for (i = 1, 2, ... n). In other words, vectors with symmetric codes such as (1, 1, 1), (2, 2, 2), ..., $(n\ n\ n)$ will produce the same zero vector.

Table 2. Extract from the calculation carried out for the 729 vectors of a nine-level inverter

$(Fa)(Fb)(Fc)$	Sa	Sb	Sc	San	Sbn	Scn	K_α	K_β	$Kref.$	Phase in degrees
(9) (1) (1)	4	-4	-4	5.33	-2.67	-2.67	6.53	0.00	6.53	0.00
(9) (2) (1)	4	-3	-4	5.00	-2.00	-3.00	6.12	0.71	6.16	6.59
(9) (3) (1)	4	-2	-4	4.67	-1.33	-3.33	5.72	1.41	5.89	13.90
(9) (4) (1)	4	-1	-4	4.33	-0.67	-3.67	5.31	2.12	5.72	21.80
(9) (5) (1)	4	0	-4	4.00	0.00	-4.00	4.90	2.83	5.66	30.02
(9) (6) (1)	4	1	-4	3.67	0.67	-4.33	4.49	3.54	5.72	38.23
(9) (7) (1)	4	2	-4	3.33	1.33	-4.67	4.08	4.24	5.89	46.13
(9) (8) (1)	4	3	-4	3.00	2.00	-5.00	3.67	4.95	6.16	53.44
(9) (9) (1)	4	4	-4	2.67	2.67	-5.33	3.27	5.66	6.53	60.03
…	…	…	…	…	…		…	…	…	…
(1) (1) (1)	-4	-4	-4	0	0	0	0	0	0	0

Table 3. Illustration of the different layers for an n-level inverter (the number of redundant vectors per layer and the number of distinct vectors per layer)

Different layers	Position number	Number of redundancies	Number of distinct vectors	Number of total vectors
$(n-1)$	6	Without	$6 \times (n-1)$	$6 \times (n-1)$
$(n-2)$	6	2	$6 \times (n-2)$	$12 \times (n-2)$
$(n-3)$	6	3	$6 \times (n-3)$	$18 \times (n-3)$
$(n-i)$	6	I	$6 \times (n-i)$	$6 \times i \times (n-i)$
…	…	…	…	…
2	6	$n-2$	$6 \times (2)$	$12 \times (n-2)$
1	6	$n-1$	$6 \times (1)$	$3 \times (n-1)$

Following the in-depth analysis of the database, we were able to establish the following general expressions for a cascaded inverter at n levels. Although derived specifically for this topology, these expressions can also be generalized to other types of multilevel inverters, regardless of their architecture (cascaded, diode-clamp, FC).

Generally, a hexagon has six sides. Thus, the total number of distinct vectors in a vector diagram associated with a multi-level inverter is given by the expression (2):

$$\text{Number of distinct vectors} = \sum_{i=1}^{n-1} 6 * (n-i) \tag{2}$$

While the total number of non-zero vectors is given by the expression (3):

$$\text{total number of non-zero vectors} = \sum_{i=1}^{n-1} 6 * i * (n-i) \tag{3}$$

The total of vectors is equal to the total number of non-zero vectors, to which we add the total number of null vectors. We will have n null vectors ranging from 111 to $n\ n\ n$ (4).

$$\textit{Total number of vectors} = \textit{ nonzero total number of vectors} + \textit{zero total number of vectors} \tag{4}$$

The direct implementation of SVPWM control from the vector diagram of an n-level inverter (with $n > 5$) is particularly complex due to the density and geometric structure of vectors in the plane $(\alpha,\ \beta)$. That is why, in practice, we generally prefer an approach of hierarchical decomposition of the diagram at n levels, gradually reducing it towards structures of lower levels, until reaching the classical representation of a 2-level inverter. This approach involves, at each stage of transition between two levels, precise knowledge: The number of transitions needed to move from one level to another in the landmark $(\alpha,\ \beta)$. And passing relations that govern the correspondence between the vectors of the different levels. Such a strategy allows for simplifying the modulation algorithm while maintaining a good accuracy of reference vector generation in the vector plane. The progressive transition from a higher level to a lower level in the vector diagram requires a precise understanding of the codes of vectors aligned with the $\alpha,\ \beta$ axes. Identifying these vectors is essential for determining the weighting coefficients $K1\alpha \ldots i\alpha \ldots\ Kn-1\alpha$ to be used during the coordinate transformation between two levels. These coefficients are critical to ensuring the continuity of the reference vector across the different layers of the diagram. Table 4 presents the codes of distinct or redundant vectors that are aligned with the α-axis. These vectors are characterized by zero phase shift and varying amplitude depending on the layer to which they belong.

• For the outermost layer $(n-1)$, there is a single distinct vector aligned with the α-axis, having the code $(n11)$. This vector, located in the most external layer, has the maximum amplitude and zero phase, representing a purely real component in the $(\alpha,\ \beta)$ reference frame.

• In layer $(n-1)$, two redundant vectors are aligned with the α-axis: $(n\ 2\ 2)$ and $(n-1)\ 1\ 1$. Although these vectors originate from different switching combinations, they share the same amplitude and a zero-phase angle.

• Generally, in the layer $(n-i)$ there are (i) redundant vectors aligned with the axis α, with codes following the pattern: $(n)\ (n-1)\ (n-1)$, $(n-1)\ (n-2)\ (n-2)$, ..., $(2,\ 1,\ 1)$. These vectors also have zero phase and decreasing amplitude as one moves toward the center of the diagram.

This consistent structuring around the α-axis is highly valuable for level transitions, reference vector synthesis, and the optimization of multilevel SVPWM algorithms.

Table 4. Vectors aligned along the Alpha axis with vector position

Layer	Number of vectors	Amplitude and phase	Starting vector aligned on the Alpha axis
$n-1$	1	$K1\alpha \times E$, 0 degrés	$(n)\ (1)\ (1)$
$n-2$	2	$K2\alpha \times E$, 0 degrés	$(n)\ (2)\ (2)$, $(n-1)\ (1)\ (1)$
$n-3$	3	$K3\alpha \times E$, 0 degrés	$(n)\ (3)\ (3)$, $(n-1)\ (2)\ (2)$, $(n-2)\ (1)\ (1)$
…	…	…	…
$n-i$	I	$Ki\alpha \times E$, 0 degrés	$(n)\ (i)\ (i)$, $(n-1)\ (i-1)\ (i-1)\ \ldots\ (n-i+1)\ (1)\ (1)$
…	…	…	…
1	$n-1$	$Kn-1\alpha \times E$, 0 degrés	$(n)\ (n-1)\ (n-1)$, $(n-1)\ (n-2)\ (n-2)\ \ldots\ (2)\ (1)\ (1)$

Table 5 presents the codes of distinct or redundant vectors that are aligned along the β-axis. These vectors are particularly important, as they correspond to purely imaginary components (vectors with a 90° phase angle) and play a critical role in symmetry analysis and the design of multilevel SVPWM control strategies.

• In the upper layer $(n-1)$, there is a single distinct vector perfectly aligned with the β-axis. This vector, located on the outermost layer, has maximum amplitude and a 90° phase shift, representing a purely imaginary component in the vector plane.

- In the $n-2$ layer, two redundant vectors are aligned (or nearly aligned) with the β-axis. These vectors share the same amplitude and maintain a phase angle close to 90°.
- In general, in the $(n-i)$ layer, there are (i) redundant vectors that can gradually align along the β-axis. These vectors exhibit a decreasing amplitude and maintain a phase angle close to 90° as they approach the center of the diagram.

This gradual alignment along the β-axis facilitates an accurate analysis of the circular distribution of vectors in the plane $(\alpha,\ \beta)$ and supports the determination of transition coefficients between layers in the hierarchical decomposition process used in multilevel SVPWM synthesis.

Table 5. Vectors aligned along the β-axis with the vector position

Layer	Number of vectors	Amplitude and phase	Starting vector aligned on the β-axis
$n-1$	1	$K1\beta \times E$, 90 degrés	$\left(\frac{n-1}{2}\right)(n)(1)$
$n-2$	2	$K2\beta \times E$, 90 degrés	$\left(\frac{n-1}{2}+1\right)(n)(2)$
$n-3$	3	$K3\beta \times E$, 90 degrés	$\left(\frac{n-1}{2}+2\right)(n)(3)$
…	…	…	…
$n-i$	I	$Ki\beta \times E$, 90 degrés	$\left(\frac{n-1}{2}+i-1\right)(n)(i)$
…	…	…	…
1	$n-1$	$Kn-1\beta \times E$, 90 degrés	$(n)(n)(n-1)$

Figure 2 illustrates a typical vector diagram of an n-level inverter, structured as concentric hexagonal layers. In these layers, we can present the different voltage vectors available in the plane $(\alpha,\ \beta)$. In this diagram, the codes of the vectors located at the vertices of the hexagon forming the outermost layer $(n-1)$ are explicitly shown. These vectors correspond to switching configurations that produce the maximum amplitudes, each oriented towards a vertex of the hexagon. In addition, the diagram highlights:

All vectors are aligned along the axes $(\alpha,\ \beta)$, with the following information for each:

Switching code $(Fa,\ Fb,\ Fc)$, Amplitude and Phase shift.

Finally, the weighting coefficients used during transitions between layers, designated by $Ki\alpha$ and $Ki\beta$, are also indicated in this figure.

The modulation of a reference vector within its vector diagram becomes particularly complex when the number of levels exceeds 5, due to the large number of vectors (n^3) and the density of their distribution in the $(\alpha,\ \beta)$ plane. To simplify the structure of the SVPWM control algorithm, it is common to use a hierarchical decomposition of the n-level vector diagram into lower-level diagrams, ultimately reducing it to the basic structure of a two-level inverter, which contains only six active vectors.

This decomposition is carried out in two main stages:

1. First, the n-level vector diagram is decomposed into six sub-diagrams, each with $+\frac{n-1}{2}+1$ levels. Graphically, each hexagon in the original n-level diagram generates six elliptical sub-hexagons $\left(\frac{n-1}{2}+1\right)$. The first sub-hexagon is oriented at an angle $H=30°$ with respect to the α-axis.

2. Second, each of these sub-diagrams is further decomposed into two-level diagrams $3(n-3)$ hexagons by applying a rotational transformation with a transition angle $L = \dfrac{\pi}{3(n-1)}$.

This fine rotation locally reorients each subdomain toward a subspace equivalent to that of a two-level inverter, for which the SVPWM algorithm is well established and easily implemented.

Figure 3 clearly illustrates this double decomposition: The angle H, corresponding to the first transition between the main hexagon of level n and the first sub hexagon of level $\dfrac{n-1}{2}+1$. And the angle L, which occurs during the second step, between this intermediate sub hexagon and the first level 2 hexagon.

The center of the first hexagon, located at the level $\dfrac{n-1}{2}+1$ aligned along the axis α is noted O $\dfrac{n-1}{2}$. and has a radius of OO$\dfrac{n-1}{2}$. Thus, to move from the center O of the top hexagon at level n to the center O $\dfrac{n-1}{2}$ of the hexagon at level $\dfrac{n-1}{2}+1$, it is enough to perform a translation of a distance equal to OO$\dfrac{n-1}{2}$. Similarly, to move from the center of the first hexagon of the level $\dfrac{n-1}{2}+1$ to the center of the first hexagon of level 2 whose center is O $n-2$ and has a radius O $n-1$O $n-2$, it suffices to perform a translation of a distance equal to O$\dfrac{n-1}{2}$ O $n-2$.

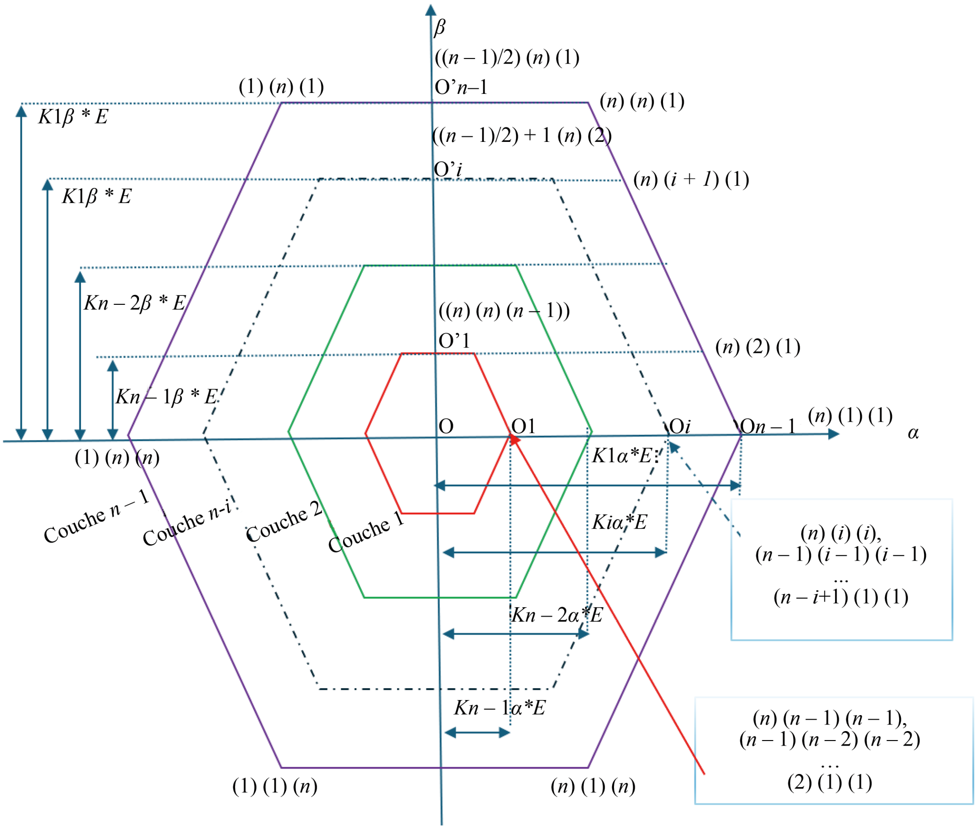

Figure 2. Structure of a vector diagram at n-levels

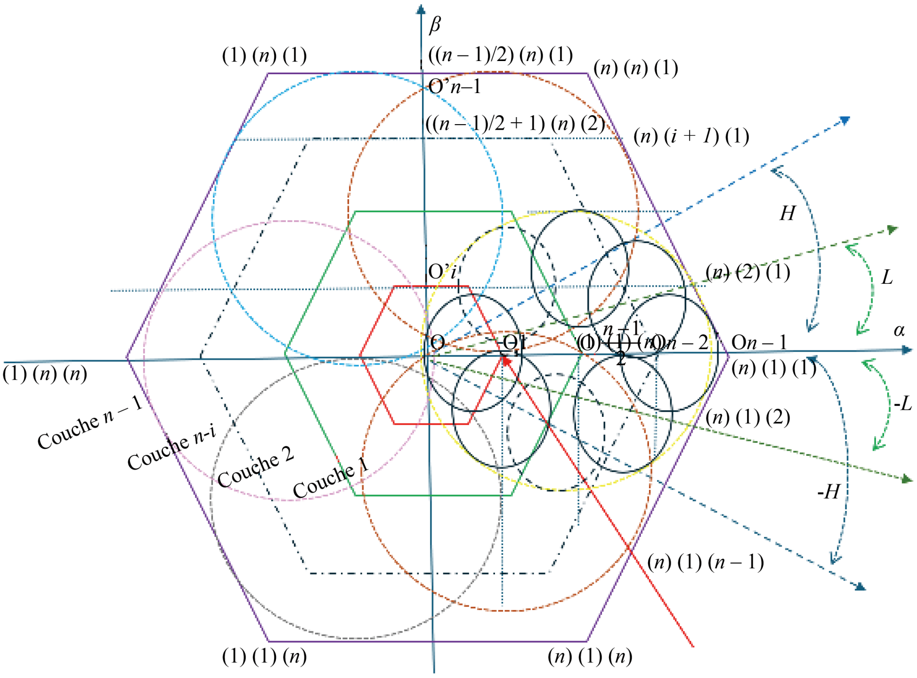

Figure 3. Transition from n-levels to other lower levels

To finalize the algorithm, it is enough to establish the relationships between the tensions in the reference frame (α, β) during the transition between the inverter at n levels and the inverter at $+\frac{n-1}{2}+1$ levels. Then, the algorithm analyses the connections between this intermediate inverter and the 2-level inverter. Always in the same frame of reference (α, β), the algorithm identifies the appropriate angular range for the angles H and L. The expressions of the different voltages are grouped in Table 6, which facilitates transitions between level n and level $+\frac{n-1}{2}+1$. In addition, this table provides the values of the H position angle for each transition. In the proposed algorithm, the values of the $K\alpha$i coefficients were rigorously selected based on the n-level vector diagram (see Figure 2).

Table 6. Table of passage from n to $\left(\frac{n-1}{2}+1\right)$

Mapping of $V_{ref}\left(\frac{n-1}{2}+1\right)$ from $V_{ref(n)}K_3 = OO\left(\frac{n-1}{2}\right) = K_\alpha\left(\frac{n-1}{2}+1\right)$			
HEX	Voltage $V_\alpha\left(\frac{n-1}{2}+1\right)$	Voltage $V_\beta\left(\frac{n-1}{2}+1\right)$	H (rad)
1	$V_{\alpha(n)} - (E)$	$V_{\beta(n)}$	$[11\pi/6\pi/6]$
2	$V_{\alpha(n)} - K_3 \cdot E\cos(\pi/3)$	$V_{\alpha(n)} - K_3 \cdot E\sin(\pi/3)$	$[\pi/6\pi/2]$
3	$V_{\alpha(n)} - K_3 \cdot E\cos(2\pi/3)$	$V_{\alpha(n)} - K_3 \cdot E\sin(2\pi/3)$	$[\pi/25\pi/6]$
4	$V_{\alpha(n)} + K_3 \cdot E$	$V_{\alpha(n)} - (K_3 \cdot E)$	$[5\pi/67\pi/6]$
5	$V_{\alpha(n)} - K_3 \cdot E\cos(4\pi/3)$	$V_{\alpha(n)} - K_3 \cdot E\sin(4\pi/3)$	$[7\pi/6\pi/2]$
6	$V_{\alpha(n)} - K_3 \cdot E\cos(5\pi/3)$	$V_{\alpha(n)} - K_3 \cdot E\sin(5\pi/3)$	$[3\pi/21\pi/6]$

The expressions of tensions in the referential (α, β) are systematically organized in Table 7, which plays a central role in managing transitions between levels $\left(\frac{n-1}{2}+1\right)$ and 2 levels. This table provides not only the analytical formulations of the voltages but also the precise values of the G position angle corresponding to each transition vector. Geometrically, each hexagon associated with the $\left(\frac{n-1}{2}+1\right)$ level is finely decomposed into $(3n-9)$ elementary hexagons of level 2. This subdivision ensures a direct and precise correspondence between the different levels of vector resolution.

Table 7. Transition table from $\left(\frac{n-1}{2}+1\right)$ level to 2 level

Passage from $V_{ref}\left(\frac{n-1}{2}+1\right)$ to $V_{ref(2)}$ Coefficient $K1 = \mathrm{OO1}$ $K2 = \mathrm{OO'1}$			
HEX	Voltage $V_{\alpha(2)}$	Voltage $V_{\beta(2)}$	L (rad)
1	$V_{\alpha}\left(\frac{n-1}{2}+1\right)-(k_1 \cdot E)$	$V_{\beta}\left(\frac{n-1}{2}+1\right)$	$\left[\frac{-\pi}{(n-1)\cdot 3} \frac{+\pi}{(n-1)\cdot 3}\right]$
2	$V_{\alpha}\left(\frac{n-1}{2}+1\right)-\left(k_2 \cdot Ecos\left(\frac{+\pi}{(n-1)\cdot 3}\right)\right)$	$V_{\alpha}\left(\frac{n-1}{2}+1\right)-\left(E \cdot k2sin\left(\frac{+\pi}{(n-1)\cdot 3}\right)\right)$	$\left[\frac{+\pi}{(n-1)\cdot 3} \frac{+2\pi}{(n-1)\cdot 3}\right]$
……	……	……	……
$3(n-3)$	$V_{\alpha}\left(\frac{n-1}{2}+1\right)-\left(k_2 \cdot Ecos\left(\frac{-\pi}{(n-1)\cdot 3}\right)\right)$	$V_{\alpha}\left(\frac{n-1}{2}+1\right)-\left(k_2 \cdot Esin\left(\frac{-\pi}{(n-1)\cdot 3}\right)\right)$	$\left[\frac{-2\pi}{(n-1)\cdot 3} \frac{-\pi}{(n-1)\cdot 3}\right]$

For example, here is a comparison between a 7-level inverter and a 9-level inverter, based on the vector diagram and the number of layers (see the vector diagrams for the 7-level and 9-level configurations).

The seven-level inverter features a particularly rich vector diagram, consisting of 343 distinct positions distributed across six main layers and a central layer (zero layer). This diagram results from all possible combinations of the voltage levels assigned to each phase, with coded values of +3, +2, +1, 0, -1, -2, -3 yielding 7 levels per phase. Among these 343 vectors, many are derived from redundant switching states. The distribution of these vectors and their associated redundancies across the layers is as follows:

Layer 6: 36 non-redundant vectors. Layer 5: 30 vectors, each with 2 redundant states. Layer 4: 24 vectors, each with 3 redundancies. Layer 3: 18 vectors, each with 4 redundancies. Layer 2: 12 vectors, each with 5 redundancies. Layer 1: 6 vectors, each with 6 redundancies. Layer 0 (central layer): contains the zero vectors, each with 7 redundancies.

In developing the switching algorithm for a 7-level inverter, a hierarchical approach is adopted, involving a progressive decomposition of the system into simpler structures. This approach is based on two key steps:

Transition from seven to four levels:

Firstly, the 7-level vector diagram is decomposed into six vector substructures equivalent to a 4-level inverter. These six substructures are arranged hexagonally; each separated from the next by a transition angle of $\pi/3$ radians.

Transition from four to two levels:

Secondly, each 4-level sub-diagram is further decomposed into a vector structure equivalent to a 2-level inverter. This decomposition results in 12 small hexagons, obtained by applying a discrete rotational transformation with an angle of $\pi/18$ radians between each hexagon.

The nine-level inverter features a particularly rich vector diagram, consisting of 729 distinct positions distributed across eight main layers and a central layer (zero layer). This diagram results from all possible combinations of the voltage levels assigned to each phase, with coded values of +4, +3, +2, +1, 0, -1, -2, -3, and -4 yielding 9 levels per phase.

Among these 729 vectors, many stem from redundant switching states. The distribution of these vectors and their redundancies across the layers is as follows:

Layer 8: 48 non-redundant vectors. Layer 7: 42 vectors, each with 2 redundancies. Layer 6: 36 vectors, each with 3 redundancies. Layer 5: 30 vectors, each with 4 redundant states. Layer 4: 24 vectors, each with 5 redundancies. Layer 3: 18 vectors, each with 6 redundancies. Layer 2: 12 vectors, each with 7 redundancies. Layer 1: 6 vectors, each with 8 redundancies. Layer 0 (central layer): contains the zero vectors, each with 9 redundancies.

In developing the switching algorithm for a 9-level inverter, a hierarchical approach is adopted, involving the progressive decomposition of the system into simpler structures. This approach is based on two key steps:

Transition from nine to five levels:

Firstly, the 9-level vector diagram is decomposed into six vector substructures equivalent to a 5-level inverter. These six substructures are arranged hexagonally; each separated from the next by a transition angle of $\pi/3$ radians.

Transition from five to two levels:

Secondly, each 5-level sub-diagram is further decomposed into a vector structure equivalent to a 2-level inverter. This decomposition results in 128 small hexagons, obtained by applying a discrete rotational transformation with an angle of $\pi/24$ radians between each hexagon.

4. Modelling of the chain of attraction

We chose to apply the SVPWM command in an attraction chain, because it has several significant advantages. First, it improves the energy efficiency of the system by reducing losses related to harmonic currents, which translates into better overall efficiency of the motor and inverter. Then, the reduction of the harmonic distortion ratio THD helps to limit thermal losses, particularly those due to the Joule effect in the motor windings, thus extending the life of the components. In addition, the reduction of harmonics attenuates mechanical vibrations and acoustic noise, limiting the excitation of unwanted resonances in the motor. Finally, a low THD improves Electromagnetic Compatibility (EMC) by reducing spurious emissions, which is essential to comply with current standards, particularly in the railway and automotive sectors.

4.1 *Electric actuator*

In this paper, we used the asynchronous machine as the actuator of the attraction chain. The equations for the voltages of the asynchronous machine indicated in the reference mark $(d,\ q)$ are as follows (5), (6), (7), (8):

$$v_{sd} = R_s \cdot i_{sd} + \frac{d\phi_{sd}}{dt} - \frac{d\theta_s}{dt} \cdot \phi_{sq} \tag{5}$$

$$v_{sq} = R_s \cdot i_{sq} + \frac{d\phi_{sq}}{dt} + \frac{d\theta_s}{dt} \cdot \phi_{sd} \tag{6}$$

$$0 = R_r \cdot i_{rd} + \frac{d\phi_{rd}}{dt} - \frac{d\theta_r}{dt} \cdot \phi_{rq} \tag{7}$$

$$0 = R_r \cdot i_{rq} + \frac{d\phi_{rq}}{dt} + \frac{d\theta_r}{dt} \cdot \phi_{rd} \tag{8}$$

The electric model is characterized by other relationships. The matrix between magnetic fluxes and electric currents is of paramount importance (9). These relationships will be exploited in the tension equations.

$$\begin{bmatrix} \phi_{sd} \\ \phi_{sq} \\ \phi_{rd} \\ \phi_{rq} \end{bmatrix} = \begin{bmatrix} L_s & 0 & M & 0 \\ 0 & L_s & 0 & M \\ M & 0 & L_r & 0 \\ 0 & M & 0 & L_r \end{bmatrix} \cdot \begin{bmatrix} i_{sd} \\ i_{sq} \\ i_{rd} \\ i_{rq} \end{bmatrix} \tag{9}$$

Finally, it can be noted that the expression of the electromagnetic torque of the asynchronous machine as a function of the components of the stator and rotor currents in the reference frame is given by (10).

$$C_e = p \cdot M \left(i_{sq} \cdot i_{rd} - i_{sd} \cdot i_{rq}\right) \tag{10}$$

Equations (5) to (10) detail the description of the electrical model of an asynchronous machine. This modelling only becomes complete after integrating the mechanical equation of the machine. It can be represented in the form of a first-order differential equation, where torque is related to mechanical angular velocity (11).

$$J \cdot \frac{d\Omega}{dt} = -K_f \cdot \Omega + \left(C_e - C_r\right) \tag{11}$$

The elements of the state model are as follows (model 1):

$$[x]^t = \begin{bmatrix} i_{sd} & i_{sq} & \phi_{rd} & \phi_{rq} \end{bmatrix}$$

$$[U]^t = \begin{bmatrix} v_{sd} & v_{sq} \end{bmatrix}$$

$$[A] = \begin{bmatrix} -\left(\frac{1}{T_s \cdot \sigma} + \frac{1-\sigma}{T_r \cdot \sigma}\right) & \omega & 1-\sigma T_r \cdot M \cdot \sigma & \frac{1-\sigma}{\sigma \cdot M} \cdot \omega_r \\ -\omega & -\left(\frac{1}{T_s \cdot \sigma} + \frac{1-\sigma}{T_r \cdot \sigma}\right) & -\frac{1-\sigma}{M \cdot \sigma} \cdot \omega_r & \frac{1-\sigma}{T_r \cdot M \cdot \sigma} \\ \frac{M}{T_r} & 0 & \frac{-1}{T_r} & \omega_g \\ 0 & \frac{M}{T_r} & -\omega_g & \frac{-1}{T_r} \end{bmatrix}$$

$$[B] = \begin{bmatrix} \frac{1}{\sigma \cdot L_s} & 0 \\ 0 & \frac{1}{\sigma \cdot L_s} \\ 0 & 0 \\ 0 & 0 \end{bmatrix} \quad \text{(Model 1)}$$

This model is used for the machine to be supplied with voltage by orienting the rotor flow along the direct axis. Indeed, it appears that the input vector is composed of voltages.

4.2 *Actuator control type*

In this article, we use the principle of the IFOC command (indirect control with field orientation). It was developed by K. Hasse. This method does not use a flow control loop and therefore does not require the use of the sensor or a flow estimator. Instead of using a flux sensor in the air gap, IFOC calculates the rotor flux vector from the angular slip velocity. Although the principle of this type of control is easily achievable, its major drawback lies precisely in the performance of the engine, which significantly degrades when faced with variations in parameters (notably the resistance of the rotor Rr) [20]. Based on the equations mentioned below and orienting the rotor flow along the direct axis, we obtain the following control equations [21]. In this case, the pulsation frequency of the angular slip (12) and the stator pulsation (12) are given by:

$$\omega_g = \frac{i_{sq}}{i_{\varphi} \cdot L_r} \cdot R_r \tag{12}$$

$$\omega_s = \omega_r + \omega_g \tag{13}$$

Using the equations below, the PI controllers can be designed to generate the reference voltages $V^*{}_{sd}$ and $V^*{}_{sq}$, as specified in (14) and (15).

$$V^*{}_{sd} = \sigma Ls \frac{di_{sd}}{dt} + \sigma Ls \left(\frac{1}{T_s \cdot \sigma} + \frac{1-\sigma}{T_r \cdot \sigma} \right) i^*{}_{sd} \tag{14}$$

$$V^*{}_{sq} = \sigma Ls \frac{di_{sq}}{dt} + \sigma Ls \left(\frac{1}{T_s \cdot \sigma} + \frac{1-\sigma}{T_r \cdot \sigma} \right) i^*{}_{sq} \tag{15}$$

The reference quadrature-axis current i^*_{sq} is calculated based on the speed control loop, as described by Equation (16):

$$i^*{}_{sq} = C_e{}^* / (p \cdot \frac{M^2}{L_r} \cdot i_{\varphi}) \tag{16}$$

Figure 4 shows the block diagram of the indirect vector control strategy. The main objective is to control torque and flux independently, similar to the operation of a separately excited DC machine. This approach is based on Field-Oriented Control (FOC), which enables the decoupled regulation of the machine's torque and flux. In this framework, the current IqsI_{qs}Iqs is used to control the torque, while the rotor flux is kept constant. After the decoupling process, the reference voltages vsd and vsq are obtained. These signals are then processed using the Park transformation, which produces the required voltage components in the $(\alpha,\ \beta)$ reference frame. These components are then used to implement the SVPWM control algorithm.

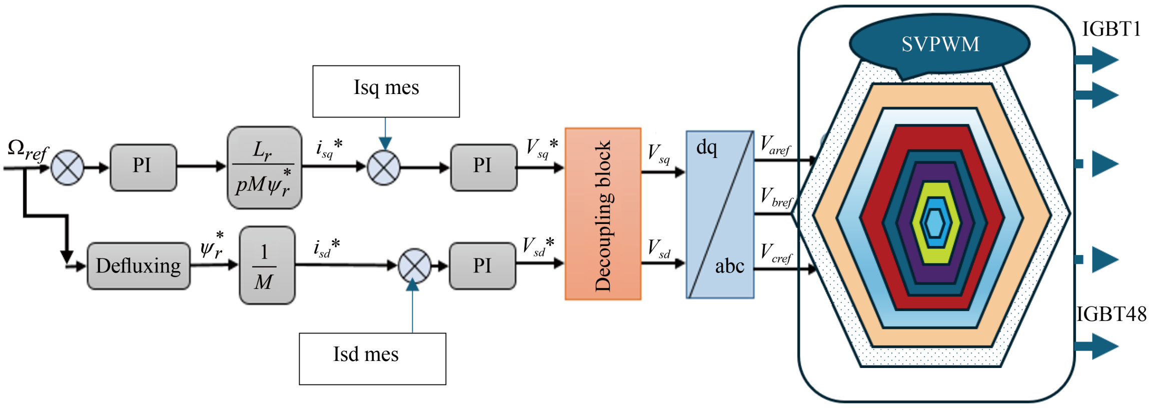

Figure 4. The figure shows the principle of indirect vector control to implement the vector SVPWM

This control was established for a nine-level inverter. For this, a complete vector diagram containing all the vectors is illustrated by Figure 5. According to the developed methodology, 729 vectors are obtained, including 217 distinct vectors named from $V1$ to $V217$. These 217 vectors have been correctly placed in the layers (ranging from 1 to 8) of the diagram, depending on their position (amplitude and phase).

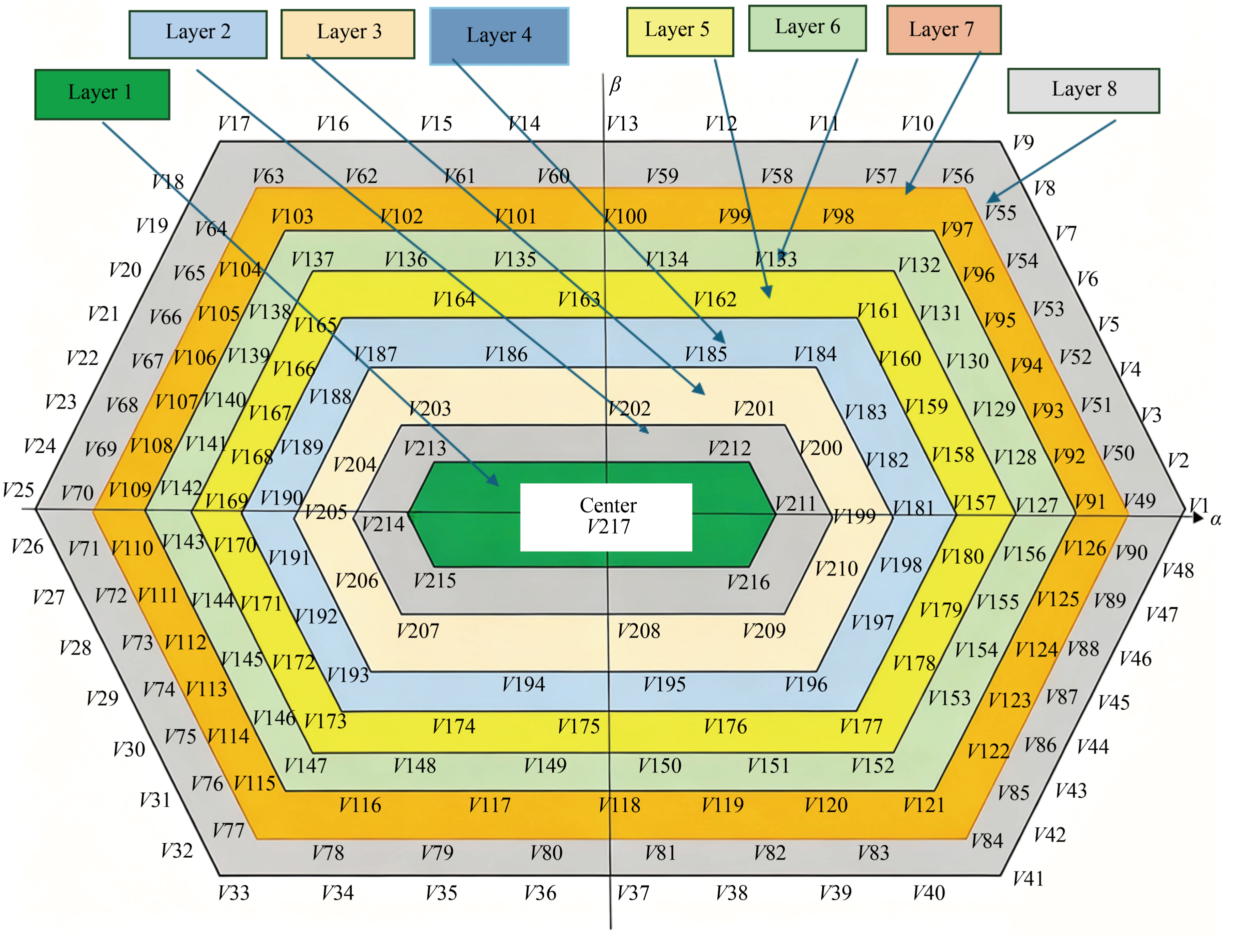

Figure 5. Vector distribution of vectors for a nine-level inverter

According to Table 8, the distinct vectors are distributed across the different layers of the vector diagram as follows:

- Layer 8: Contains 48 distinct vectors, ranging from $V1$ to $V48$. The first vector is $V1(911)$ and the last one is $V48(212)$.
- Layer 7: Comprises 42 distinct vectors, from $V49$ to $V90$. The first vector is $V49(922$ or $811)$, with one redundancy, and the last is $V90(923$ or $812)$.
- Layer 6: Contains 36 distinct vectors, from $V91$ to $V126$. The first vector is $V91(933$ or 822 or $711)$, with two redundancies, and the last is $V126(934$ or 823 or $712)$.
- Layer 5: Includes 30 distinct vectors, ranging from $V127$ to $V156$. The first vector is $V127(944$ or 833 or 722 or $611)$, with three redundancies, and the last is $V156(945$ or 834 or 723 or $612)$.
- Layer 4: Consists of 24 distinct vectors, from $V157$ to $V180$. The first vector is $V157(955$ or 844 or 733 or 622 or $511)$, with four redundancies, and the last is $V180(956$ or 845 or 734 or 623 or $512)$.

- Layer 3: Contains 18 distinct vectors, from $V181$ to $V198$. The first vector is $V181$(966 or 855 or 744 or 633 or 522 or 411), with five redundancies, and the last is $V198$(967 or 856 or 745 or 634 or 523 or 412).
- Layer 2: Comprises 12 distinct vectors, from $V199$ to $V210$. The first vector is $V199$(977 or 866 or 755 or 644 or 533 or 422 or 311), with six redundancies, and the last is $V210$(978 or 867 or 756 or 645 or 534 or 423 or 312).
- Layer 1: Finally, this layer contains 6 distinct vectors, from $V211$ to $V216$. The first vector is $V211$(988 or 877 or 766 or 655 or 544 or 433 or 322 or 211), with seven redundancies, and the last is $V216$($V216$ (989 or 878 or 767 or 656 or 545 or 434 or 323 or 212).

Table 8. Table containing all the vectors of a nine-level inverter

Layer	Number of vectors ranging from 1 to 729
8	$V1$(911), $V2$(921), $V3$(931), $V4$(941), $V5$(951), $V6$(961), $V7$(971), $V8$(981), $V9$(991), $V10$(891), $V11$(791), $V12$(691), $V13$(591), $V14$(491), $V15$(391), $V16$(291), $V17$(191), $V18$(192), $V19$(193), $V20$(194), $V21$(195), $V22$(196), $V23$(197), $V24$(198), $V25$(199), $V26$(189), V27(179), $V28$(169), $V29$(159), $V30$(149), $V31$(139), $V32$(129), $V33$(119), $V34$(219), $V35$(319), $V36$(419), $V37$(519), $V38$(619), $V39$(719), $V40$(819), $V41$(919), $V42$(918), $V43$(917), $V44$(916), $V45$(915), $V46$(914), $V47$(913), $V48$(912)
7	$V49$(922; 811), $V50$(932; 821), $V51$(942; 831), $V52$(952; 841), $V53$(962; 851), $V54$(972; 861), $V55$(982; 871), $V56$(992, 881), $V57$(892; 781), $V58$(792; 681), $V59$(692; 581), $V60$(592; 481), $V61$(492; 381), $V62$(392; 281), $V63$(292; 181), $V64$(293; 182), $V65$(294; 183), $V66$(295; 184), $V67$(296; 185), $V68$(297; 186), $V69$(298; 187), $V70$(299; 188), $V71$(289; 178), $V72$(279; 168), $V73$(269; 158), $V74$(259; 148), $V75$(249; 138), $V76$(239; 128), $V77$(229; 118), $V78$(329; 218), $V79$(429; 318), $V80$(529; 418), $V81$(629; 518), $V82$(729; 618), $V83$(829; 718), $V84$(929; 818), $V85$(928; 817), $V86$(927; 816), $V87$(926; 815), $V88$(925; 814), $V89$(924; 813), $V90$(923; 812)
6	$V91$(933; 822; 711), $V92$(943 ; 832 ; 721), $V93$(953; 842; 731), $V94$(963; 852; 741), $V95$(973; 862; 751), $V96$(983; 872; 761), $V97$(993; 882; 771), $V98$(893, 782; 671), $V99$(793; 682; 571), $V100$(693; 582; 471), $V101$(593; 482; 371), $V102$(493; 382; 271), $V103$(393; 282; 171), $V104$(494; 283; 172), $V105$(495; 284; 173), $V106$(396; 285; 174), $V107$(397; 286; 175), $V108$(398; 287; 176), $V109$(399; 288; 177), $V110$(389; 278; 167), $V111$(379; 268; 157), $V112$(369; 258; 147), $V113$(359; 248; 137), $V114$(349; 238; 127), $V115$(339; 288; 117), $V116$(439; 328; 217), $V117$(539; 428; 317), $V118$(639; 528; 417), $V119$(739; 628; 517), $V120$(839; 728; 617), $V121$(939; 828; 717), $V122$(938; 827, 716), $V123$(826; 138; 715), $V124$(825; 718; 714), $V125$(824; 118; 713), $V126$(934; 823; 712)
5	$V127$(944; 833; 722; 611), $V128$(954; 843; 732; 621), $V129$(964; 853; 742; 631), $V130$(974; 863; 752; 641), $V131$(984; 873; 762; 651), $V132$(994; 883; 772; 661), $V133$(894; 783; 672; 561), $V134$(794, 683 ; 572; 461), $V135$(694; 583; 472; 361), $V136$(594; 483; 372; 261), $V137$(494; 383; 272; 161), $V138$(495; 384; 273; 162), $V139$(496; 385; 274; 163), $V140$(497; 386; 275; 164), $V141$(498; 87; 276; 165), $V142$(988; 877; 766; 655), $V143$(489; 378; 267; 165), $V144$(479; 368; 257; 146), $V145$(469; 358; 247; 136), $V146$(459; 348; 237; 126), $V147$(449; 338; 227; 116), $V148$(549; 438; 327; 216), $V149$(649; 538; 427; 316), $V150$(749; 638; 527; 416), $V151$(849; 738; 627;516), $V152$(949; 838; 727; 616), $V153$(948; 837; 726; 615), $V154$(947; 836; 725; 614), $V155$(946; 835; 724; 613), $V156$(945;834, 723;612)

Table 8. (cont.)

Layer	Number of vectors ranging from 1 to 729
4	$V157$(955; 844; 733; 622; 511), $V158$(965; 854; 743; 632.521), $V159$(975; 864; 753; 642.531), $V160$(985 ; 874; 763; 652, 541), $V161$(995; 884; 773; 662; 551), $V162$(895; 784; 673; 562; 451), $V163$(795; 684; 672; 561), $V164$(695, 584; 473; 362, 251), $V165$(595; 484; 373; 262, 151), $V166$(596; 485; 374; 263; 152), $V167$(597; 486; 375; 264, 153), $V168$(598; 487; 376; 265; 154), $V169$(599; 488; 377; 266; 155), $V170$(589; 478; 367; 256; 145), $V171$(579; 468; 357; 246; 135), $V172$(569; 458; 347; 236; 125), $V173$(559; 448; 337; 226; 115), $V174$(659 ;548; 437; 326; 215), $V175$(759; 648; 537; 426; 315), $V176$(859; 748; 637; 526; 415), $V177$(959; 848; 737; 626; 515), $V178$(958; 847; 736; 625, 514), $V179$(957; 846; 735; 624; 513), $V180$(956; 845; 734; 623; 512)
3	$V181$(966; 855; 744; 633; 522; 411); $V182$(976; 865; 754; 643; 532; 421); $V183$(986; 875; 764; 653; 542; 431); $V184$(996; 885; 774; 663; 552; 441); $V185$(896; 785; 674; 563; 452; 341); $V186$(796; 685; 544; 433; 322; 211); $V187$(696; 585; 474; 363; 252; 141); $V188$(697; 586; 475; 363; 252; 141); $V189$(698; 587; 476; 365; 254; 143); $V190$(699; 588; 477; 366; 255; 144); $V191$(689; 578; 467; 356; 245; 134); $V192$(679; 568; 457 346; 234; 123); $V193$(669; 558; 447; 336; 225; 115); $V194$(769; 658; 547; 436; 325; 214); $V195$(869; 758; 647; 536; 425; 314); $V196$(969; 858; 747; 636; 525; 414); $V197$(968; 857; 746; 635; 524; 413); $V198$(967; 856; 745; 634; 523; 412)
2	$V199$(977; 866; 755; 644; 533; 422; 311); $V200$(987; 876; 765; 654; 543; 432; 321); $V201$(997; 886; 775; 664; 553; 442; 331); $V202$(897; 786; 675; 564; 453; 342; 231); $V203$(797; 686; 575; 464; 353; 242; 131); $V204$(798; 687; 576; 465; 354; 243; 132); $V205$(799; 688; 577; 466; 355; 244; 133); $V206$(789; 678; 567; 456; 345; 234; 123); $V207$(779; 668; 557; 646; 435; 324; 213); $V208$(879; 768; 657; 546; 435; 324; 213); $V209$(979; 868; 757; 646; 535; 424; 313); $V210$(978; 867; 756; 645; 534; 423; 312)
1	$V211$(988; 877; 766; 655; 544; 433; 322; 211); $V212$(998; 887; 776; 665; 554; 443; 332; 221); $V213$(898; 787; 676; 565; 454; 343; 232.121); $V214$(899; 788; 677; 566; 455; 344; 233; 122); $V215$(889; 778; 667; 556; 445; 334; 223; 112); $V216$(989; 878; 767; 656; 545; 434; 323; 212)
0	$V217$(999; 888, 777; 666; 555, 444, 333, 222; 111)

4.3 *Type of supply for the attraction chain*

In this work, we used photovoltaic generators to power an asynchronous machine via a multi-level converter. Practical studies on photovoltaic cells show that the current generated by a cell directly depends on the illumination. On the one hand, the higher the light intensity, the greater the current produced by the cell. On the other hand, the open circuit voltage is influenced by the quality of the material used and the type of junction ($P-N$) of the cell. This voltage represents the maximum potential that the cell can reach when no current flows. The equations that characterize a PV module are (17)-(20) [22].

$$I = I_{ph} - I_D - I_P \tag{17}$$

$$I_D = I_0 \left(\exp\left(\frac{V}{Vt} \right) - 1 \right) \tag{18}$$

$$Vt = \frac{K.T}{q} \tag{19}$$

$$I_p = \frac{V + R_s.I}{R_p} \tag{20}$$

The relationship between I and V is given by (21):

$$I = I_{ph} - I_0\left(\exp\left(\frac{V + R_s I}{a.Vt}\right) - 1\right) - \frac{V + R_s.I}{R_p} \tag{21}$$

The photocurrent I_{ph} characterizes the spectral response of the photovoltaic cell and varies with environmental conditions, particularly ambient temperature and solar irradiance G. It is mathematically defined by Equation (22):

$$I_{ph} = \frac{G}{Gr}\left(Iscr + Ki(T - Tr)\right) \tag{22}$$

The saturation current I0 is expressed by (23):

$$I_0 = I_{or}\left(\frac{T}{Tr}\right)^3 \cdot \exp\left(\frac{qEg}{Ak}\left(\frac{1}{Tr} - \frac{1}{T}\right)\right) \tag{23}$$

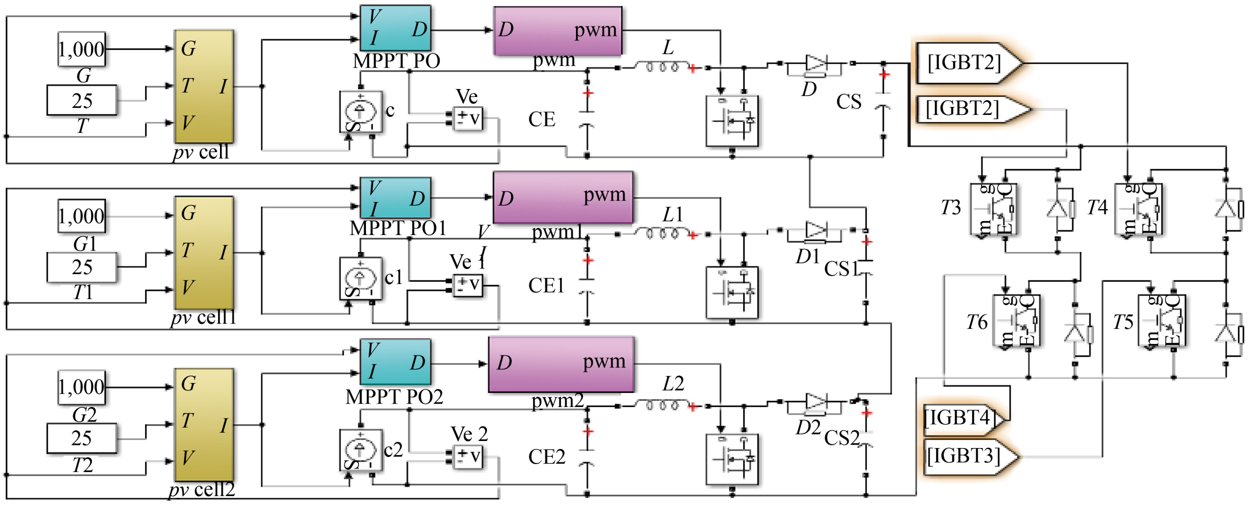

Figure 6. Block diagram of photovoltaic generators associated with step-up converters to supply a bridge of the converter at nine levels

To efficiently transfer the electrical energy generated by PV cells, amplification converters are used in conjunction with Maximum Power Point Tracking (MPPT) controllers. These controllers operate at very high switching frequencies, typically between 20 kHz and 80 kHz [23], depending on the power level. Such high-frequency operation offers several advantages, including the reduction in size of magnetic components and capacitors, thus allowing the integration of MPPT control into compact and efficient systems. In this context, it is often reasonable to assume an ideal lossless DC-DC converter, which implies that the total power produced by the photovoltaic generator is fully transferred to the load. In this study, the photovoltaic source consists of three solar panels. In this work, we adopted a modular design, where each PV module is connected to its own DC/DC boost converter. These boost converters are then connected in series (see Figure

6). The output of this modular configuration powers a single bridge of the multi-level inverter. Since our configuration requires twelve bridges, we need twelve identical photovoltaic sources. This topology offers several advantages. Mainly, it reduces the required filtering capacity at the output of photovoltaic cells, resulting in improved efficiency and reduced costs.

Table 9 presents the characteristics of a panel, which are always provided by reference to nominal or standard test conditions for temperature and solar irradiation.

Table 9. PV specifications (1 KW/M^2, 25 °C)

S.No	Parameters	Value
K-pv	Boltzman constant	1.38065×10^{-23}
q-pv	Charge of electron	1.602×10^{-19}
Iscn-pv	Nominal SC Currentè	8.21 A
Vocn-pv	Nominal OC voltage	32.9 V
Kv-pv	Temperature Voltage Constant	0.123
Ki-pv	Temperature current constant	0.003
Ns-pv	Nbr of series-connected cells	48
Tr-pv	Nominal temperature	298
Gr-pv	Nominal irradiance	1,050 W/m^2

5. Simulation results

The system comprising photovoltaic panels, a DC-DC converter, a cascaded multilevel inverter, and an induction motor was simulated. The specifications of the asynchronous machine used are: $L_s = 0.973$ H, $L_r = 0.3558$ H, $Rs = 6.8$ Ω, $R_r = 5.4$ Ω; $M = 0.39$ H, $p = 2$, $J = 0.02$ Kgm^2; $K_f = 0.0025$ Nm/rad/s, $P = 1$ Kw. The simulation was conducted for 4 seconds, with the magnetizing flux reference maintained at a constant value. To evaluate the performance of our system, we subjected it to irradiance variations of approximately 1,000 W/m^2, under a constant ambient temperature of 25 °C.

- From 0 to 0.4 seconds, the angular velocity is maintained at 120 rad/s.
- At 0.4 seconds, the angular velocity reference is set to 120 rad/s.

Figure 7 illustrates the output voltage waveform of the nine-level inverter, while Figure 8 provides a close-up view of the interval between 0.22 and 0.36 seconds. The Fast Fourier Transform (FFT) analysis shows that the total harmonic distortion (THD) for the five-level waveforms is 12%. This THD value is important for evaluating the power quality delivered by the nine-level converter and its subsequent impact on the performance of the induction motor.

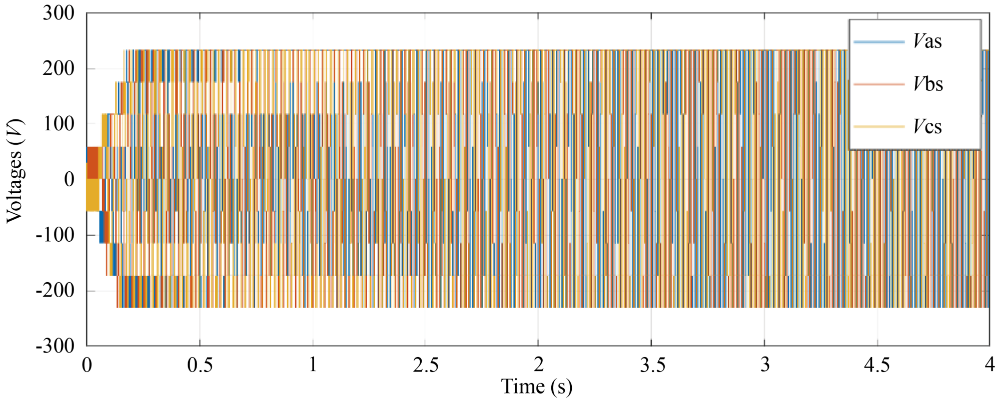

Figure 7. Simple voltage waveforms (a b c)

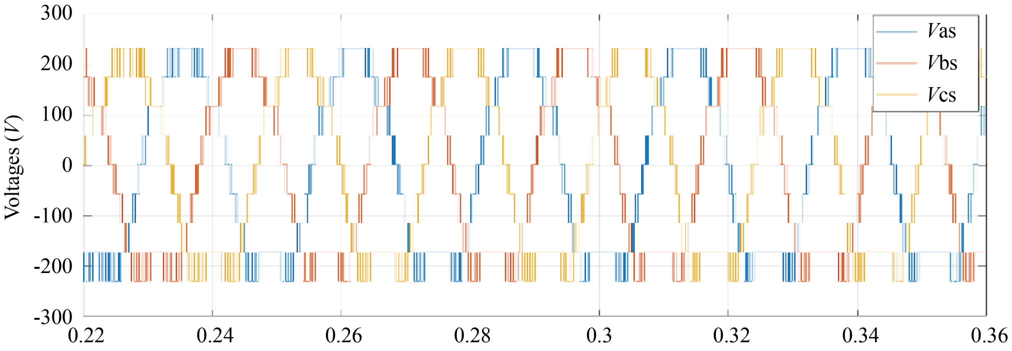

Figure 8. Waveforms of compound voltages between (0.22 s to 0.36 s)

The photovoltaic conversion chain was tested at a temperature of 25 °C and an irradiation level of 1,000 W/m^2. Figure 9 illustrates the characteristic that binds the voltage and the current obtained at the output of a solar cell. The curve clearly shows the proper functioning of the MPPT controller. This MPPT controller operates at very high frequencies, generally in the range of 20 kHz to 80 kHz (in our simulation, we chose 20 kHz).

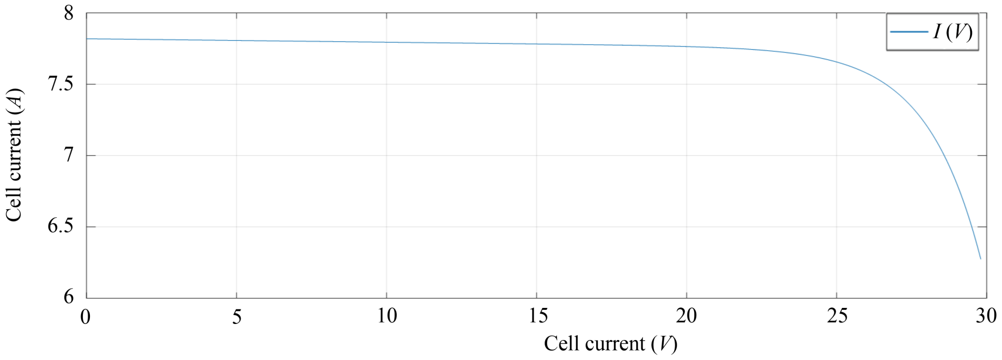

Figure 9. $I-V$ characteristic of a single photovoltaic cell

The output current waveforms of the asynchronous motor powered by a 9-level converter using a photovoltaic system based on boost converters are shown in Figure 10, with a zoom presented in Figure 11. These waveforms show the evolution of currents in the induction motor in response to the power provided by the 9-level inverter. The analysis of currents, especially in transient conditions, is crucial for understanding engine performance, notably:

- Current stability: The stability of currents is essential to avoid overloads and ensure optimal operation of the motor.
- Harmonics: The study of waveforms can also reveal the presence of harmonics, which can affect equipment efficiency and lifetime.

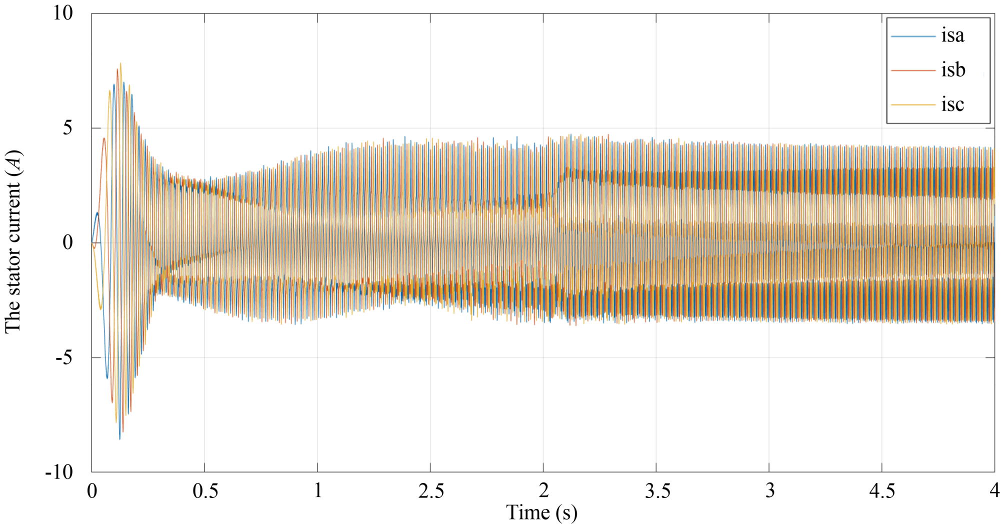

Figure 10. Stator current waveforms

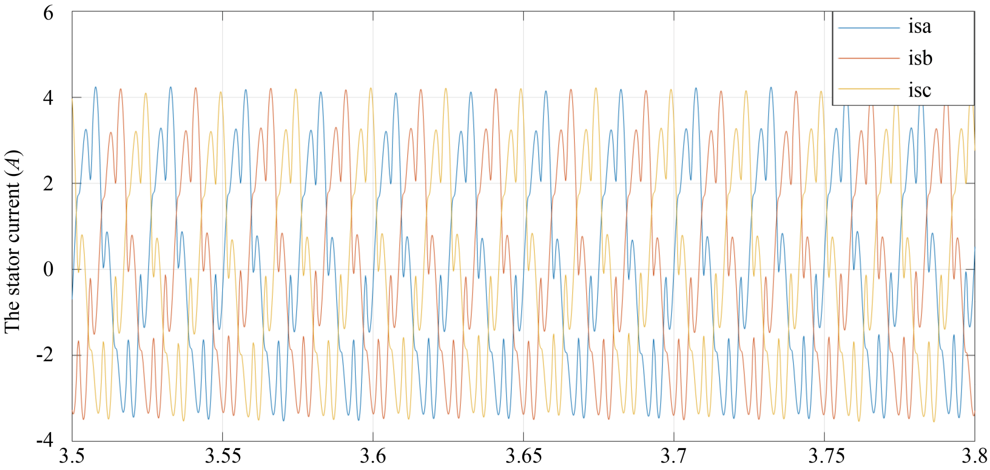

Figure 11. Stator current waveforms (3.5 s to 3.8 s)

Figure 12 illustrates the evolution of the rotational speed curves, showing both the reference and the actual values expressed in rad/s. We observe an increase in speed followed by stabilization at the set speed.

Figure 13 depicts the responses of the electromagnetic torque and the load torque when the system operates with photovoltaic sources of varying values. The torque begins to increase from 0 Nm and stabilizes at 6 Nm starting from t = 2 s. The rise of the electromagnetic torque to 6 Nm demonstrates the motor's capability to meet the load requirements.

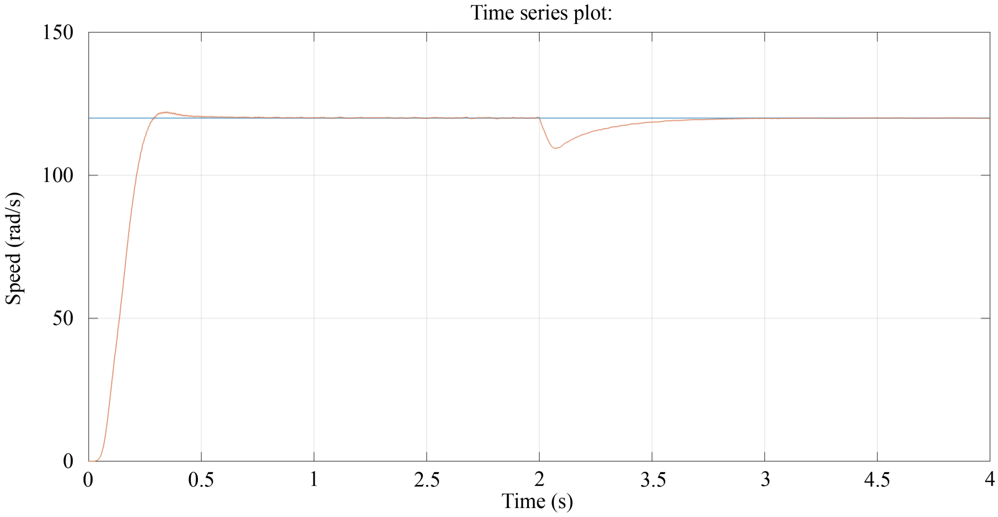

Figure 12. Actual and reference speed

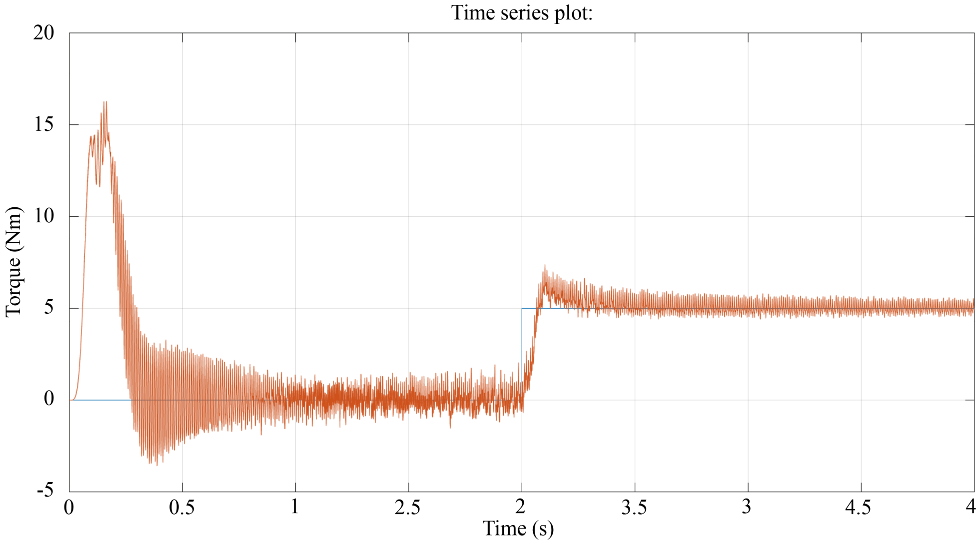

Figure 13. Electromagnetic torque and load torque

6. Conclusion

The study and the simulation results have demonstrated that the SVPWM algorithms developed for controlling an inverter at n levels are valid and efficient for configurations ranging from 5 to 15 levels. The proposed algorithms have been shown to be both efficient and adaptable to various operating conditions, highlighting their potential for practical applications, notably in the field of renewable energy systems. By leveraging the SVPWM control technique, the inverter successfully generates output voltages at nine levels, resulting in a significant reduction of the harmonic spectrum to about 12%. The new methodology developed for the SVPWM control algorithms was validated through simulation. The obtained control signals are promising, allowing us to improve the quality of the signals supplied to the motor. The developed controllers demonstrate satisfactory performance under various operating conditions, ensuring precise and responsive system monitoring. Simulation results confirmed that the photovoltaic sources are optimized around the Maximum Power Point (MPP), confirming the system's efficiency in terms of energy production. The study demonstrated that the proposed model is both effective and adaptable to different operating conditions, highlighting its potential for practical applications in the field of renewable energy systems. The results confirm both the effectiveness and reliability of the approach.

Conflict of interest

The author declares no competing financial interest.

References

[1] Youssef MZ, Woronowicz K, Aditya K, Azeez NA, Williamson SS. Design and development of an efficient multilevel DC/AC traction inverter for railway transportation electrification. *IEEE Transactions on Power Electronics*. 2016; 31(4): 3036-3042. Availavle from: https://doi.org/10.1109/TPEL.2015.2448353.

[2] Mukherjee N, Tricoli P. Modular multilevel converter-based supercapacitor integration strategies and their comparative evaluation for railway traction drive systems. In: *2015 17th European Conference on Power Electronics and Applications*. Geneva, Switzerland: IEEE; 2015. p.8-10.

[3] Wang K, Zheng Z, Xu L, Li Y. Neutral-point voltage balancing method for five-level NPC inverters based on carrier-overlapped PWM. *IEEE Transactions on Power Electronics*. 2021; 36(2): 1428-1440. Availavle from: https://doi.org/10.1109/TPEL.2020.3006960.

[4] Ruderman A, Reznikov B, Margaliot M. Simple analysis of a flying capacitor converter voltage balance dynamics for DC modulation. In: *2008 13th International Power Electronics and Motion Control Conference*. Poznan, Poland: IEEE; 2008. p.1-3.

[5] Sami M, Mallick MA. Cascaded H-bridge 11-level multilevel inverter. *International Journal of Engineering Research and Technology*. 2021; 10(6). Available from: https://www.ijert.org/research/cascaded-H-bridge-11-level-multilevel-inverter-IJERTV10IS060099.pdf [Accessed 14th July 2025].

[6] Rout K, Sahu O, Mishra S. A comparative analysis of different topologies of an eleven level inverter for solar power applications. In: *2018 International Conference on Recent Innovations in Electrical, Electronics and Communication Engineering*. Bhubaneswar, India: IEEE; 2018. p.27-28.

[7] Oumaymah E, Abdellah O, Omar B, Lhoussain EB. NPC five level inverter using SVPWM for grid-connected hybrid wind-photovoltaic generation system. *Advances in Science, Technology and Engineering Systems Journal*. 2020; 5(6): 981-987. Availavle from: https://doi.org/10.25046/aj0506117.

[8] Franquelo LG, Leon JI, Dominguez E. Recent advances in high-power industrial applications. In: *2010 IEEE International Symposium on Industrial Electronics*. Bari, Italy: IEEE; 2010. p.4-7.

[9] El Bourhichi S, Oukassi A, El Adnani M. Indirect vector control of induction motor using a five-level cascaded H-bridge inverter. In: *2018 International Symposium on Advanced Electrical and Communication Technologies*. Kenitra, Morocco: IEEE; 2018. p.21-23.

[10] Elamri O, Oukassi A, El Bahir L, El Idrissi Z. Combined vector and direct controls based on five-level inverter for high performance of IM drive. *World Electric Vehicle Journal*. 2022; 13(1): 17. Availavle from: https://doi.org/10.3390/wevj13010017.

[11] Hossain ML. *Control of a Multilevel Inverter for Wind Energy Conversion System with Energy Storage and Condition Monitoring Options*. Curtin University; 2020.

[12] Oukassi A, El Bourhichi S, Eladnani M. Indirect vector control of induction motor fed by a five-level cascaded H-bridge inverter using the PV generators. In: *2020 International Conference on Electrical and Information Technologies*. Rabat, Morocco: IEEE; 2020. p.4-6.

[13] Subarnan G, Venkatesan VJ. Multi carrier based multilevel inverter with minimal harmonic distortion. *International Journal of Power Electronics and Drive Systems*. 2015; 6(2): 253-260. Availavle from: https://doi.org/10.11591/ijpeds.v6i2.7193.

[14] Prasad E, Sudhakar A, Kumar V. Simulation of five-level inverter fed PMSM based on fast SVPWM. In: *2012 IEEE International Conference on Power Electronics, Drives and Energy Systems*. Bengaluru, India: IEEE; 2012. p.16-19.

[15] Kamani PL, Patel RK, Kathiria MK, Majithiya DP, Brahmkhatri JH. Implementing selective harmonic elimination in multilevel inverters with optimal dc source. *e-Prime-Advances in Electrical Engineering, Electronics and Energy*. 2024; 8: 100622. Availavle from: https://doi.org/10.1016/j.prime.2024.100622.

[16] Rathore S, Kirar MK, Singh BS. Simulation of cascaded H-bridge multilevel inverter using PD, POD, APOD techniques. *Electrical and Computer Engineering: An International Journal*. 2015; 4(3): 27-41. Availavle from: https://doi.org/10.14810/ecij.2015.4303.

[17] Ahmed I, Borghate VB. Simplified space vector modulation technique for seven-level cascaded H-bridge inverter. *IET Power Electronics*. 2014; 7(3): 604-613. Availavle from: https://doi.org/10.1049/iet-pel.2013.0135.

[18] Oukassi A, Boulghasoul Z, El Bahir L. Hybrid PLM and ADRC control for sensorless induction motor drive with nine-level converter employing SVPWM. *Contemporary Mathematics*. 2024; 5(4): 4441-4468. Availavle from: https://doi.org/10.37256/cm.5420245034.

[19] Busireddy HK, Lokhande MM, Karasani RR, Borghate VB. A modified space vector PWM approach for nine-level cascaded H-bridge inverter. *Arabian Journal for Science and Engineering*. 2018; 44(3): 2131-2149. Availavle from: https://doi.org/10.1007/s13369-018-3363-3.

[20] Oukassi A, Elbourhichi S. Sensorless indirect control of induction motor fed by a multi-level inverter with consideration of variation in rotor and stator resistances. In: *2020 7th International Conference on Electrical and Electronics Engineering*. Antalya, Turkey: IEEE; 2020. p.14-16.

[21] Blaschke F. The principle of field orientation as applied to the new transvector closed loop control system for rotating field machines. *Siemens Review*. 1972; 34(5): 217-220.

[22] El Bahir L, Hassboun T, Driss YA, El Adnani M. Estimator of local solar irradiation based on a PV model. In: *2015 International Conference on Electrical and Information Technologies*. Marrakech, Morocco: IEEE; 2015. p.25-27.

[23] Arrouf M, Bouguechal N. Vector control of an induction motor fed by a photovoltaic generator. *Applied Energy*. 2003; 74(1-2): 159-167. Availavle from: https://doi.org/10.1016/S0306-2619(02)00142-3.